Volume 15
Number 6
21 March 2025
Pages 1679–2050

# Catalysis Science & Technology

rsc.li/catalysis

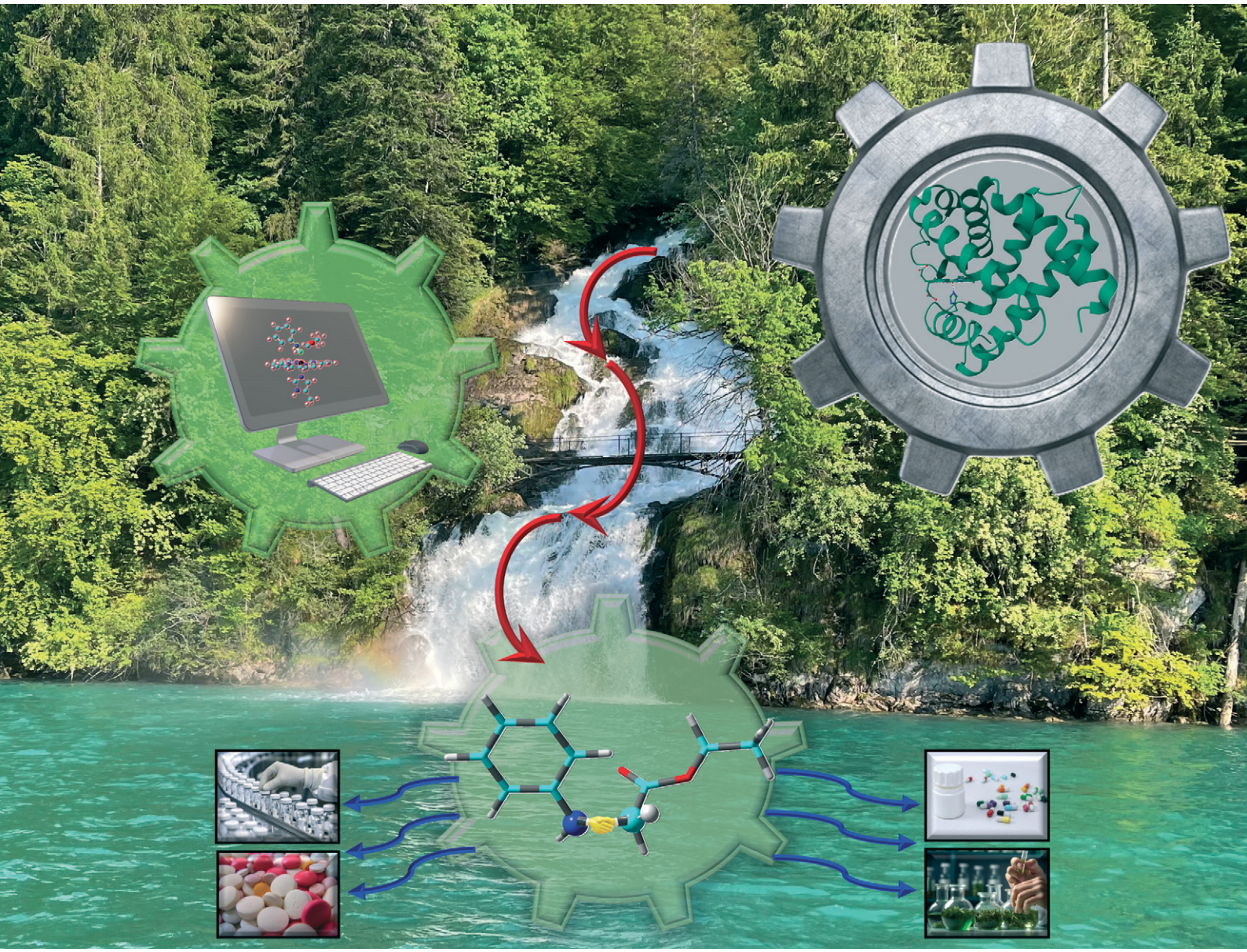

ISSN 2044-4761

ROYAL SOCIETY OF CHEMISTRY

**PAPER**

Rudi Fasan, Yong Zhang *et al.*

A comprehensive mechanistic investigation of sustainable carbene N–H insertion catalyzed by engineered His-ligated heme proteins

Catalysis Science & Technology

ROYAL SOCIETY OF CHEMISTRY

PAPER

View Article Online
View Journal | View Issue



Cite this: *Catal. Sci. Technol.*, 2025, **15**, 1802

# A comprehensive mechanistic investigation of sustainable carbene N–H insertion catalyzed by engineered His-ligated heme proteins†

Rahul L. Khade,[a] Ronald Daisuke Adukure,[b] Xinyi Zhao,[a] Carolyn Wang,[a] Rudi Fasan *[b] and Yong Zhang *[a]

Engineered heme proteins possess excellent biocatalytic carbene N–H insertion abilities for sustainable synthesis, and most of them have His as the Fe axial ligand. However, information on the basic reaction mechanisms is limited, and ground states of heme carbenes involved in the prior computational mechanistic studies are under debate. A comprehensive quantum chemical reaction pathway study was performed for the heme model with a His analogue as the axial ligand and carbene from the widely used precursor ethyl diazoacetate with aniline as the substrate. The ground state of this heme carbene was calculated by the high-level complete active space self-consistent field (CASSCF) approach, which shows a closed-shell singlet that is consistent with many experimental works. Based on this, DFT calculations of ten main reaction pathways were compared. Results showed that the most favorable pathway involved the initial formation of the metal-bound ylide, followed by a concerted rearrangement/dissociation transition state to form the free enol, which then underwent a water-assisted proton transfer process to yield the final N–H insertion product. This computational prediction was validated *via* new experimental data using His-ligated myoglobin variants with different types of carbenes. Overall, this is the first comprehensive computational mechanistic study of heme carbene N–H insertions, particularly for neutral His ligated heme proteins and the first high-level CASSCF confirmation of the ground state of the used heme carbene. The experimental results are also the first in this field. Overall, these results build a solid basis for the proposed reaction mechanism to facilitate future biocatalytic carbene N–H insertion studies.

Received 15th August 2024,
Accepted 10th January 2025

DOI: 10.1039/d4cy00999a

rsc.li/catalysis



## 1. Introduction

Carbenoid N–H insertion is a powerful approach to provide a concise synthetic route for α-amino acid derivatives, α-amino ketones, alkaloids, N-heterocyclic compounds, and other bioactive molecules.[1–17] It has also been used for bioconjugation purposes.[18–21] Initially, iron porphyrins were found and further developed to be used as effective catalysts for this reaction.[22–26] More recently, engineered Fe-containing heme proteins, such as cytochrome P450/P411,[27–29] myoglobin (Mb),[30–35] cytochrome c,[36,37] YfeX (peroxidase),[38] protoglobin,[39] and neuroglobin,[40] were explored in a wide range of carbenoid N–H insertions. Clearly, except for P450/P411s, all other experimental studies, which consist of ~80% work in this field, employed His-ligated heme protein variants (mostly Mb-based), which exhibit promising biocatalytic results with up to 99% yield[32,34,40] and excellent chemoselectivity.[30,33,36] These His-ligated heme biocatalysts can work under aerobic conditions with reductants[31,35] and be extended to aliphatic amine substrates besides aromatic amines[33] and effect asymmetric N–H insertions[34] with up to 99% ee.[37] In addition, all these engineered heme biocatalysts work under ambient conditions such as room temperature and aqueous solutions. The features of biocompatibility and no toxicity of these biocatalytic proteins along with the use of the most abundant and inexpensive transition metal (Fe) support their potential use in sustainable chemical synthesis for new C–N bonds.

Compared to the above-mentioned large body of experimental advances in this area, computational mechanistic work is relatively scarce.[28,29,36,37,40–42] While the protein environment effects on chemoselectivity[36] and stereoselectivity[28,29,37] have been well elucidated computationally, there is only a small set of basic reaction mechanism information of heme carbene N–H insertions, for which density functional theory (DFT) studies have been employed to understand these Fe(II)-based biocatalytic transformations. In 2016, a DFT study was reported that

[a] *Department of Chemistry and Chemical Biology, Stevens Institute of Technology, 1 Castle Point Terrace, Hoboken, NJ 07030, USA. E-mail: yong.zhang@stevens.edu*
[b] *Department of Chemistry and Biochemistry, University of Texas at Dallas, Richardson, TX 75080, USA. E-mail: rudi.fasan@utdallas.edu*

† Electronic supplementary information (ESI) available. See DOI: https://doi.org/10.1039/d4cy00999a

provided some initial mechanistic information. For instance, the hydrogen atom transfer (HAT) pathway (see Scheme 1 with L = Cys; only the first step was calculated) was found to be less favorable than the first step of ylide formation in Scheme 1 for aniline N–H insertion catalyzed by cytochrome P450 with a Cys axial ligand.[41] With the Fe(II) metal bound ylide, a concerted dissociation/rearrangement was calculated to be kinetically more favorable than the sequential pathway, which is similar to **Pathway-II** and **Pathway-III** branch **a** up to only $\mathbf{Int_{NC}}$ (a free enol dissociated from heme) in Scheme 1, respectively. A direct proton transfer **Pathway-I** was found to be of higher energy. In contrast, the dissociation **Pathway-III** branch **b** was adopted in more recent computational studies for Ser-ligated heme N–H insertions with a cyclic carbene,[28,29] which offer interesting insights into the subsequent free ylide pathway to the final product (different from the above-mentioned enol pathway for the acyclic carbene [:$CHCO_2Et$]).[41] That work also uncovered the roles of water-assisted proton transfer. Compared with these two computational studies of heme proteins with negatively charged ligands (Cys and Ser), a recent study for the His-ligated heme (cytochrome c) with carbene [:$CMeCO_2Et$][36] revealed a comparison of the first ylide formation step with a direct hydrogen transfer mechanism (similar to the hydride transfer pathway in Scheme 1, as found for Si–H[36,43] and C–H insertions[44]). Clearly, each of the prior computational mechanistic works only studied a few possibilities and limited steps, which show that different mechanisms may be favored for biocatalysts with different axial ligands. So, there has been no comprehensive complete mechanism study from heme carbene to the final product formation, as shown in Scheme 1 (to be described in detail later), particularly for the neutral His ligand. Recent reports of heme protein reactions show that the axial ligand can modulate reactivity[43,45–47] and sometimes change preferred pathways.[28,48,49] So, it is important to study

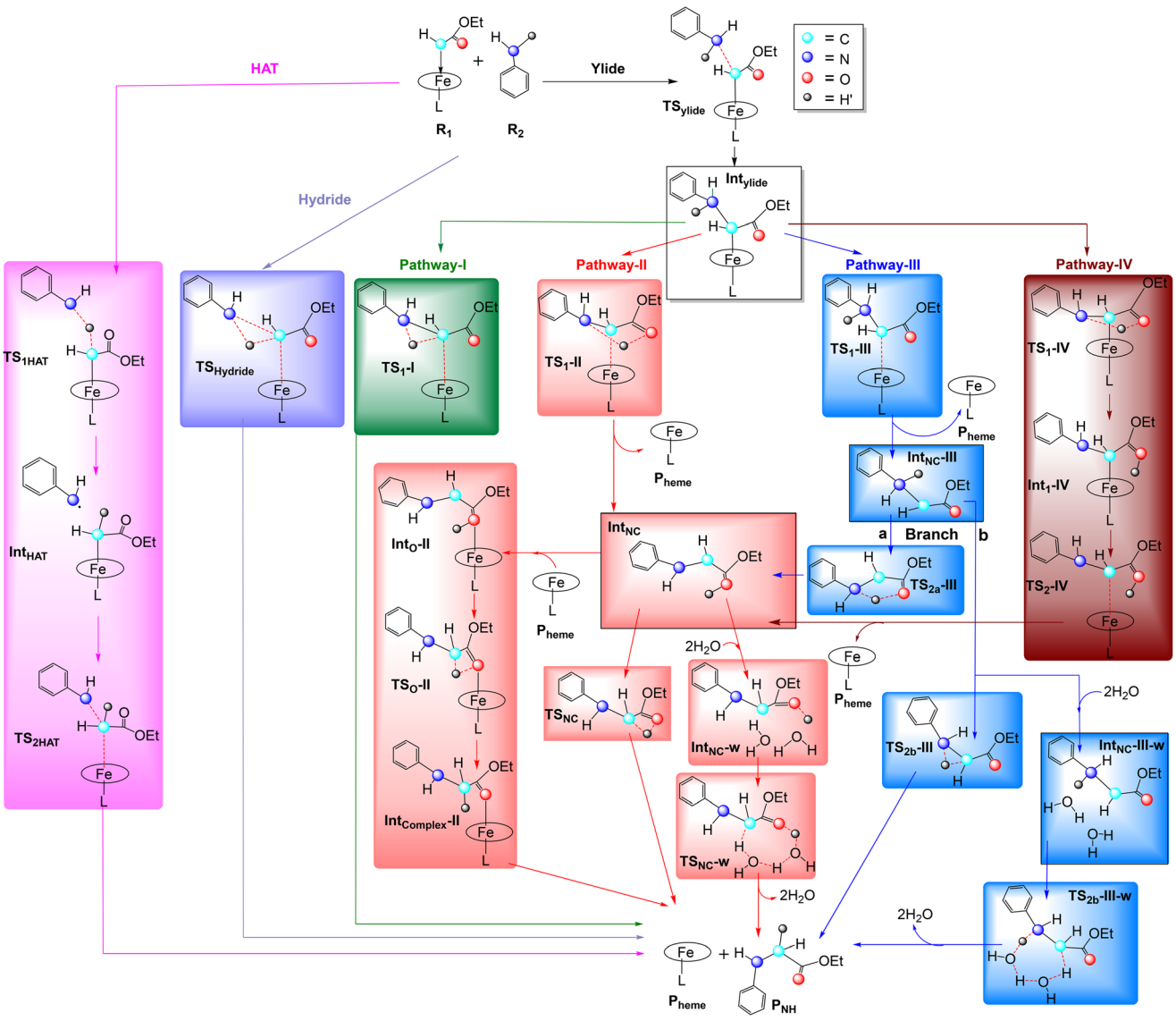


**Scheme 1** Different N–H insertion pathways. L = axial ligand. H′: hydrogen, in grey, to be transferred from aniline to carbene carbon.

the full reaction pathways for His-ligated heme catalysts, which constitute ~80% of the experimentally used engineered heme proteins for N–H insertions.[30–40]

In addition, all these N–H insertion pathway DFT calculations[28,29,36,41] used the open shell singlet (OSS) as the ground state for heme carbenes. However, it is known that certain DFT methods may not be accurate for some electronic structure calculations. Our recent studies show that only the close shell singlet (CSS) of Fe(II)-heme carbene systems yielded accurate predictions of experimental X-ray, Mössbauer and NMR spectroscopic properties.[44,50] This CSS feature was further supported by a more recent experimental study using X-ray absorption near edge spectroscopy.[51] Moreover, the CSS feature was confirmed in high-level multireference quantum chemical calculations using the complete active space self-consistent field (CASSCF) method for iron porphyrins with carbene [:$CMeCO_2Et$] and several axial ligands *N*-methylimidazole, methyl thiolate, and hydroxide,[52] which are analogues of His, Cys, and Ser ligands. This CSS feature also enabled the successful predictions of a wide range of experimental heme carbene reactivities of cyclopropanations and Si–H and C–H insertions.[43,44,47]

Considering the above mechanistic problems and the experimental prevalence (~80%) of His-ligated heme proteins particularly Mb variants[30–40] in N–H insertions, we chose to perform a comprehensive mechanistic investigation, as shown in Scheme 1 with L = His for the heme carbene N–H insertion reaction of model [Fe(Por)(5-MeIm)($CHCO_2Et$)] (**$R_1$**; $Fe^{II}$(Por): non-substituted porphyrin; 5-MeIm: 5-methylimidazole for His, as used recently[43,46,47,53]) derived from the widely used carbene precursor ethyl diazoacetate (EDA) in this field[31,32,35,38,40] with aniline (**$R_2$**) substrate, using the DFT method, which enabled accurate predictions of experimental properties of heme carbenes and their reactivities, stereoselectivities, regioselectivities, and chemoselectivities;[43,44,46,47,50,53–55] see Experimental details section 2.2. The electronic structure of this heme carbene **$R_1$** was first investigated using the high-level CASSCF method to compare CSS, OSS, and other spin states not reported before to validate the ground state for subsequent DFT pathway studies. As shown in Scheme 1, this is the first systematic pathway study for His-ligated heme catalyzed N-H insertion from heme carbene (**$R_1$**) and substrate (**$R_2$**) to the final product (**$P_{NH}$**) and recycled catalyst (**$P_{heme}$**). In addition, there are several mechanistic features in Scheme 1 that have not been studied before: 1) the comparison of ylide with HAT and hydride pathways; 2) the comparison of four ylide pathway branches: a) concerted direct proton transfer from aniline nitrogen to carbene carbon with C–N bond formation to form final products (**Pathway-I**), b) concerted dissociation of iron porphyrin (**$P_{heme}$**) with the rearrangement of proton from aniline N to carbonyl O to form an enol intermediate **$Int_{NC}$** (**Pathway-II**), c) dissociation to form the free ylide **$Int_{NC}$-III** (**Pathway-III**), d) rearrangement to form the metal-bound enol **$Int_1$-IV**, then dissociate to release free enol **$Int_{NC}$** (**Pathway-IV**); 3) the study of three possible pathways from free enol to final products, including the metal-coordinated one *via* transition state **$TS_O$-II** and metal-free pathways with and without water assistance through **$TS_{NC}$** and **$TS_{NC}$-w** respectively; 4) the comparison of indirect and direct pathways from the free ylide to final product for the acyclic carbene: a) rearrange to free enol *via* **$TS_{2a}$-III** first, then proceed to enol pathways, b) two direct pathways with and without water assistance through **$TS_{2b}$-III** and **$TS_{2b}$-III-w**, respectively. Overall, there are ten main pathways investigated in this work, with the most favorable mechanism further validated by new experimental results. It should also be noted that there is no prior experimental mechanistic study regarding the basic reaction mechanism in this field. Although the protein environment is important to determine the final biocatalytic reaction, our work, here, as the first study of the His-ligated heme protein catalyzed N–H insertion is focused on the effect of cofactor structure on reaction mechanism as done previously in this field.[28,29,36,41]

## 2. Experimental details

### 2.1 CASSCF calculations

For heme carbene **$R_1$**, its DFT optimized geometry was used with 6-311G(d) for Fe and its coordinated atoms and 6-31G(d) for all other atoms. For the active space for the CASSCF calculations, as in a recent CASSCF study of similar heme carbenes,[52] we also used the same option of 12 electrons in 12 orbitals, which are the largest level among recent CASSCF studies of heme carbene and nitrene systems[56,57] as well as other metal complexes.[58,59] Similarly, our studied active space also started from the examination of natural orbitals and consists of frontier five Fe 3d orbitals $3d_{xy}$, $3d_{yz}$, $3_{xz}$, $3_{x^2-y^2}$, $3d_{z^2}$, and $\pi/\pi^*$ and $\sigma$ carbene orbitals involved in Fe–C bonding, see Fig. 1. Our CASSCF(12,12) calculations used the $N_{Root}$ = 5 with the state average option using equal weights. More details of the configuration state functions (CSFs) with >1% weight for each studied state are discussed in ESI† section S2. We used the Gaussian 16 program for these calculations.[60]

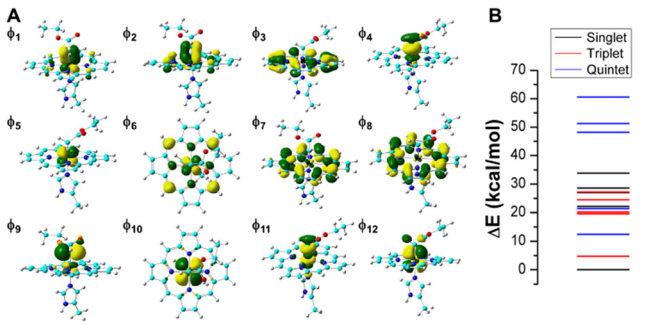


Fig. 1 A) Active space molecular orbitals (MOs) $\phi_{1-12}$ of $R_1$. Contour values = ±0.04 au. Atom colors: N – blue, O – red, C – cyan, H – grey, Fe – black. B) Energy levels of the studied singlet, triplet, and quintet spin states.

### 2.2 DFT calculations

All the models investigated in this work were subject to full geometry optimizations without any symmetry constraints using the PCM method[61] with a dielectric constant of 4.0 to simulate the protein environment effect as done previously.[28,29,36,41,43–48,53–55,62–64] Compared to this value, additional calculations using a high-end dielectric constant value of 78.3553 for the pure aqueous solvent environment (~20-fold increase) only increased the reaction barrier by 1.22 kcal $mol^{-1}$ for the heme carbene formation reaction. As a protein contains many non-polar residues and is much less polar than water, the impact on the absolute value of the reaction barrier will be much less than this value. In fact, the current use of the dielectric constant of 4.0 enabled accurate quantitative predictions of experimental heme reaction barriers (*e.g.*, an average error of 0.11 kcal $mol^{-1}$ (ref. 48)) and experimental non-heme reaction barriers (*e.g.*, an error of 0.36 kcal $mol^{-1}$ (ref. 64)) besides reproducing reactivity trends of a number of biocatalytic heme carbene and nitrene transfer reactions.[43,45,47,53–55]

Geometry optimization was conducted using a range-separated hybrid DFT method with dispersion corrections, ωB97XD,[65] with the effective core potential (ECP) basis LanL2DZ[66] for iron and the triple-zeta basis 6-311G(d) for all other elements, based on its accurate predictions of reactions involving heme carbenes.[43,44,46,47,50,53–55] This basis set is larger than the ones used in recent computational studies of heme N–H insertions.[36,41,67,68] The use of a much larger 6-311++G(2d,2p) basis for all non-metal atoms was found to yield similar results for heme carbene reactions[44] and thus further support the efficient use of the current basis set here. The use of an ECP basis for metals is common in many reaction studies involving transition metal carbenoids, such as Ir/Ru/Th carbenes.[69–71] The advantage of an ECP basis is the inclusion of a relativistic effect basically absent in an all-electron basis set. In addition, it is available for all transition metals, which may allow direct comparisons of the effects of a vast amount of metal centers. The alternative use of an all-electron basis for the metal center[47] was recently found to yield qualitatively the same conclusions of geometric, electronic, and energetic features for heme carbene reactions and therefore supports the use of the LanL2DZ basis here, which may help direct comparisons with late transition metals in future studies, for which ECP basis is more readily available and commonly used. The frequency analysis was used to verify the nature of the stationary points on respective potential energy surfaces and to provide zero-point energy corrected electronic energies ($E_{ZPE}$'s), enthalpies ($H$'s), and Gibbs free energies ($G$'s) at 1 atm and experimental reaction temperature, *i.e.*, room temperature. All the DFT calculations were performed using the Gaussian 09 program[72] as done in recent works on heme carbene reactions.[43–47,50,53–55] The atomic charges and spin densities are from the natural population analysis (NPA) and Mulliken schemes implemented in Gaussian 09. Intrinsic reaction coordinate calculations were done to prove the connection between each TS and its corresponding stationary states. We also performed a detailed conformation and spin state study for relevant species, as given in ESI,† and then selected the most favorable ones in the reaction pathway discussion here. Except for the CSS states, spin unrestricted DFT calculations were performed, including the OSS states, for which we used the broken-symmetry method.[73]

### 2.3 Reagents and analytical methods

All chemicals and reagents were purchased from commercial suppliers (Sigma Aldrich, TCI Chemicals) and used without any further purification.

### 2.4 Protein expression and purification

Wild-type Mb and engineered Mb variants were cloned and expressed in *E. coli* C41(DE3) cells as described previously.[34] Briefly, cells were grown in TB medium (ampicillin, 100 mg $L^{-1}$) at 37 °C (180 rpm) until OD600 reached 0.8–1.0. Cells were then induced with 0.25 mM β-D-1-thiogalactopyranoside (IPTG) and 0.3 mM δ-aminolevulinic acid (ALA). After induction, cultures were shaken at 27 °C (180 rpm), harvested after 20 h by centrifugation (4000 rpm, 20 min, 4 °C) and resuspended in an Ni-NTA lysis buffer (50 mM KPi, 250 mM NaCl, 10 mM histidine, pH 8.0). Resuspended cells were frozen and stored at −80 °C. Cell suspensions were thawed at room temperature, lysed by sonication, and clarified by centrifugation (14 000 rpm, 50 min, 4 °C). The clarified lysate was transferred to a Ni-NTA column equilibrated with the Ni-NTA lysis buffer. The protein was washed with the Ni-NTA wash buffer (50 mM KPi, 250 mM NaCl, 20 mM histidine, pH 8.0). Proteins were eluted with the Ni-NTA elution buffer (50 mM KPi, 250 mM NaCl, 250 mM histidine, pH 7.0). After buffer exchange (50 mM KPi, pH 7.0), the proteins were stored at +4 °C. Myoglobin concentration was determined by UV/vis spectroscopy using an extinction coefficient of $\varepsilon_{410}$ = 157 $mM^{-1}$ $cm^{-1}$.

### 2.5 N–H insertion reactions

Under standard reaction conditions, reactions were carried out at a 400 μL scale using 10 μM myoglobin, 5 mM amine, 10 mM diazo compound, with or without 50 mM DMPO and 10 mM sodium dithionite. In a typical procedure, in an anaerobic chamber, a solution containing the desired myoglobin variant was mixed with a solution of sodium dithionite in nitrogen-purged potassium phosphate buffer (50 mM, pH 8.0). Reactions were initiated by the addition of 10% DMF or DMPO (50 mM stock in DMF), amine (400 mM stock solution in EtOH), followed by the addition of the diazo compound (400 mM stock solution in EtOH), and the reaction mixtures were stirred in the chamber for 1 h at room temperature. For product analysis, an internal standard (20 μL of benzodioxole at 100 mM in ethanol) was added to the reaction mixture, followed by extraction with dichloromethane (400 μL) and analysis by GC-FID.

### 2.6 Synthetic procedures and product characterization

Detailed procedures and characterizations for the synthesis of N–H insertion products are provided in the ESI.†

## 3. Results and discussion

### 3.1 CASSCF study of heme carbene

To obtain a rigorous electronic structure of $\mathbf{R_1}$, we first investigated different spin states ($S$ = 0, 1 and 2) using CASSCF calculations. The active space orbitals in our CASSCF(12,12) (12 electrons in 12 active orbitals) calculation are shown in Fig. 1A. Because each spin state can have different contributions or resonance structures of the fragments in $\mathbf{R_1}$, each of the five lowest energy levels for $S$ = 0, 1, 2 from CASSCF calculations are shown in Fig. 1B.

As shown in Fig. 1B and Tables S2–S4,† the CSS state with a single predominant contribution from the CSS configuration state function that has all frontier occupied orbitals with double occupancy (*i.e.*, paired) is the overall lowest energy spin state for this His-ligated heme with the

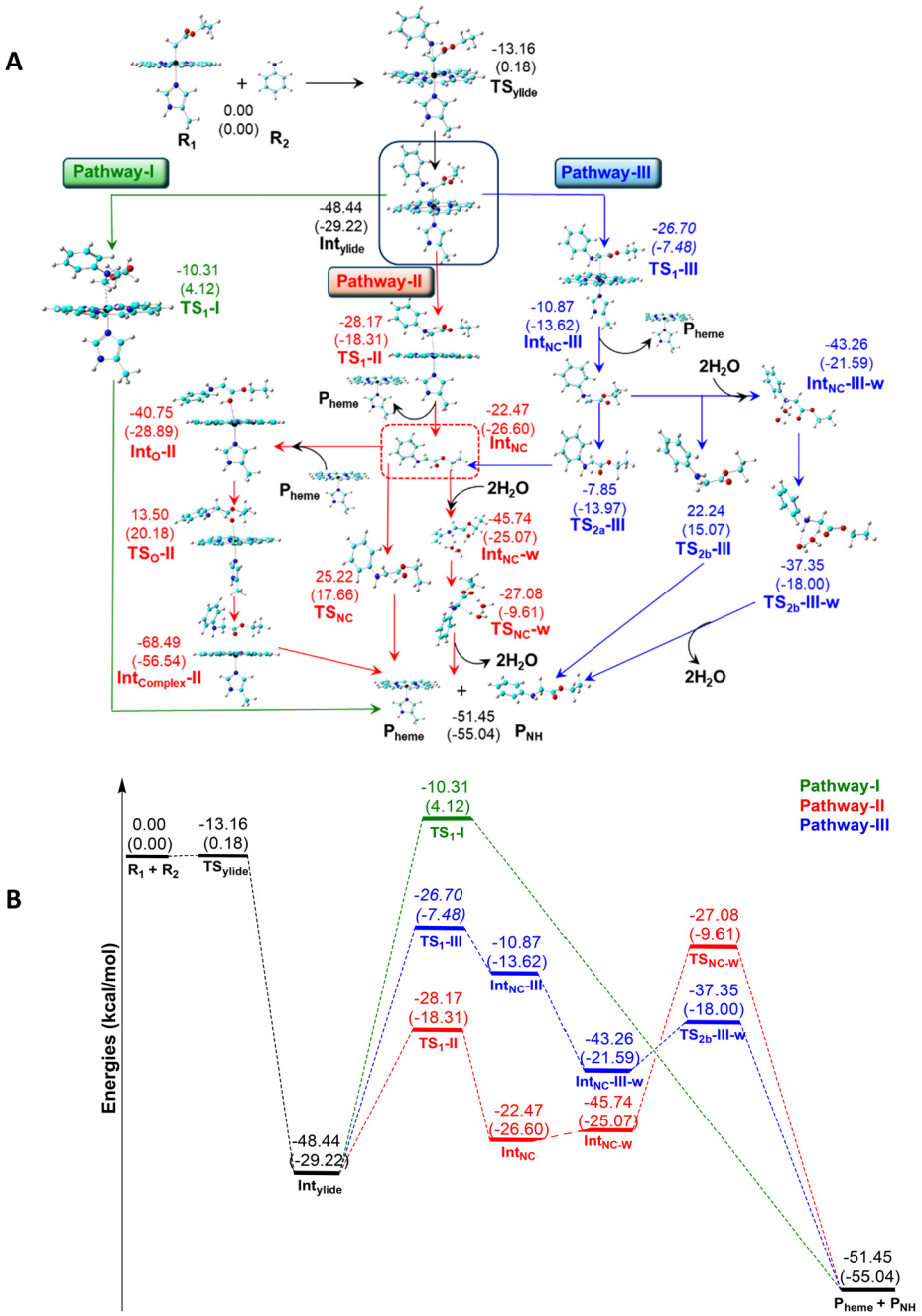


**Fig. 2** A) Energy diagrams for the successfully located ylide pathways of heme-carbene-catalyzed N–H insertions. B) Schematic energy profile for the most favourable steps in **Pathway-I**, **-II** and **-III**. The energy levels are based on $\Delta G$. Relative $\Delta E$ and $\Delta G$ energies (in kcal mol$^{-1}$) are outside and inside the parenthesis, respectively. $\Delta E/\Delta G$ results for $\mathbf{TS_1}$**-III** shown in italics are from potential energy scan calculations; see ESI† for details.

 

carbene derived from the widely used ethyl diazoacetate. All other higher-energy singlets exhibit OSS features (see ESI† for details). The lowest OSS state has an $\Delta E$ of 22.14 kcal mol$^{-1}$, higher than the CSS ground state. This trend is the same as found in the previous CASSCF result of a similar heme carbene[52] and different from previous DFT pathway studies in this field.[28,29,36,41] This is not unexpected as DFT is a single determinant method; thus, it is difficult to handle electronic states with multi-reference nature. In fact, most of the calculated electronic states involve a strong mixture of MOs with different characters, see ESI† section S2. According to our CASSCF calculations, the next energy level above the CSS ground state is a triplet (it is of $\Delta E$ 4.70 kcal mol$^{-1}$ higher, Table S3†), which is lower than the most stable OSS state by 17.44 kcal mol$^{-1}$. This trend is also consistent with the recently reported CASSCF result of a similar heme carbene.[52] We further examined the quintet states and found that the lowest $S$ = 2 state is of even a higher $\Delta E$ of 12.46 kcal mol$^{-1}$ than CSS, see Table S4.† These results support that this heme carbene has CSS as the overall ground state as found experimentally and computationally for heme carbenes.[43,44,47,50,51] So, this CSS ground state is used for $\mathbf{R_1}$ in subsequent pathway studies.

### 3.2 Ylide pathways

We first investigated ylide pathways in Scheme 1. A detailed conformation and spin state study was done for relevant species (see ESI† for details) to provide the most favorable conformations and spin states in the reaction pathway discussion here. As shown in Fig. 2, it is kinetically and thermodynamically very favorable for $\mathbf{R_1}$ to react with aniline ($\mathbf{R_2}$) to form the C–N bond in the ylide intermediate ($\mathbf{Int_{ylide}}$) *via* transition state ($\mathbf{TS_{ylide}}$), a common step for all four ylide pathways.

**Pathway-I** is the concerted pathway with direct proton H′ transfer from N to C along with the Fe–C bond dissociation in the transition state $\mathbf{TS_1}$**-I** to form the product $\mathbf{P_{NH}}$ and regenerate the biocatalyst $\mathbf{P_{heme}}$. Its relative energy to the starting reactants is 4.12 kcal mol$^{-1}$, and its relative barrier to $\mathbf{Int_{ylide}}$ ($\Delta G^{\ddagger}$: 33.34 kcal mol$^{-1}$) is the highest among all studied ylide pathways (to be discussed in detail later), see Fig. 2. This trend for the neutral ligand His ligated heme carbene N–H insertion is the same as found for the heme with a negatively charged Cys ligand.[41] The intrinsic reaction coordinate (IRC) calculations for $\mathbf{TS_1}$**-I** (see Fig. S4†) confirmed that it is connected with $\mathbf{Int_{ylide}}$ (not the reactant complex, *i.e.*, the C–N bond in ylide is maintained) and the product complex of $\mathbf{P_{NH}}$ and $\mathbf{P_{heme}}$.

**Pathway-II** is also concerted but it involves the rearrangement of ylide to enol (aniline first transfers H′ to carbonyl oxygen) along with dissociation of the Fe–C bond. Its transition state $\mathbf{TS_1}$**-II** to form the enol intermediate ($\mathbf{Int_{NC}}$) has a relative barrier to $\mathbf{Int_{ylide}}$ ($\Delta G^{\ddagger}$: 10.91 kcal mol$^{-1}$) that is much lower than **Pathway-I**. This step is similar to that proposed for the Cys-ligated heme with the same carbene.[41] For $\mathbf{TS_1}$**-II**, the Fe–C bond length is 2.658 Å, while it is 2.206 Å for $\mathbf{TS_1}$**-I**, as shown in Table S9.† A longer Fe–C bond length in $\mathbf{TS_1}$**-II** in **Pathway-II** leads to more favorable bond dissociation compared to $\mathbf{TS_1}$**-I** in **Pathway-I**. Along with the Fe–C bond dissociation in both pathways, the N–H′ bond in aniline breaks, and H′ is transferred to either the carbonyl oxygen to form a new O–H′ bond in $\mathbf{TS_1}$**-II** or the carbene's carbon to generate the new C–H′ bond in $\mathbf{TS_1}$**-I**. Here, the O–H′ bond formation is more favorable as compared to the C–H′ bond formation because oxygen is more electronegative than carbon. Therefore, both the bond dissociation and new bond formation parts contribute to a lower barrier of $\mathbf{TS_1}$**-II** as compared to $\mathbf{TS_1}$**-I**.

However, the subsequent steps from $\mathbf{Int_{NC}}$ to the final N–H insertion product $\mathbf{P_{NH}}$ have not been reported before. For this reason, we investigated three possible subsequent pathways.

Since $\mathbf{Int_{NC}}$ is released in the active site with heme nearby, we first studied if the coordination of Fe to carbonyl O could facilitate the rearrangement or transfer of H′ on O to C as in $\mathbf{P_{NH}}$, see Scheme 1. The metal–O coordinated rearrangement mechanism was previously studied in a non-heme carbene system[74] but has not been explored for heme carbenes before. It starts with the coordination step to generate intermediate $\mathbf{Int_O}$**-II** and then proceed *via* the transition state $\mathbf{TS_O}$**-II** to form another intermediate complex, $\mathbf{Int_{Complex}}$**-II**, which eventually forms products. As shown in Scheme S1,† from $\mathbf{Int_{NC}}$ with an energy of −26.60 kcal mol$^{-1}$, the coordination stabilizes $\mathbf{Int_O}$**-II** by 2.29 kcal mol$^{-1}$. However, $\mathbf{TS_O}$**-II** is significantly uphill by 49.07 kcal mol$^{-1}$ to be 20.18 kcal mol$^{-1}$ with respect to starting reactants, although the subsequent $\mathbf{Int_{Complex}}$**-II** is thermodynamically very favorable. So, this metal-coordinated enol transformation has a relative $\Delta G^{\ddagger}$ of 46.78 kcal mol$^{-1}$ from $\mathbf{Int_{NC}}$, which is very high.

We then studied the direct transfer mechanism for enol proton in $\mathbf{Int_{NC}}$ to carbene's carbon to yield the final product. The relative barrier for this transition state $\mathbf{TS_{NC}}$ is 44.26 kcal mol$^{-1}$, which is still high, although better than the metal-coordinated one.

In light of the beneficial effect of water assistance in proton transfer for ylide in recent computational works of negatively charged ligand ligated heme carbene N–H insertions[28] and the availability of water in such biocatalytic environments, we investigated this transition state in the cases of one water and two water molecules and compared with the above water-free result. It was found that the two-water model involving a concerted rearrangement of H′ from carbonyl oxygen to carbene carbon *via* the two-water cascade and then to product formation, as shown in Scheme 1, is the best; see ESI† section S5 for details. Its ($\mathbf{TS_{NC\text{-}W}}$) relative barrier from $\mathbf{Int_{NC}}$ is decreased to 16.99 kcal mol$^{-1}$ in contrast with the water-free case of 44.26 kcal mol$^{-1}$. This trend of water assistance for enol rearrangement is similar to the ylide proton transfer mechanisms calculated recently.[28] But, a comparison of the water-assisted proton transfer

mechanism for enol with metal-assisted and water-free pathways here is reported for the first time in this field.

As shown in Fig. 2, the most favorable $\mathbf{TS_{NC\text{-}W}}$ for enol transformation to the final product has a $\Delta G$ of −9.61 kcal mol$^{-1}$ with respect to the starting reactants. Compared to the first transition state in **Pathway-II**, $\mathbf{TS_1}$**-II**, this step is of higher energy and thus is the rate-determining step (RDS). Therefore, **Pathway-II** is more favorable than **Pathway-I** because $\mathbf{TS_{NC\text{-}W}}$ has a lower $\Delta G$ than $\mathbf{TS_1}$**-I** by 13.73 kcal mol$^{-1}$ (Fig. 2).

As seen from Scheme 1, **Pathway-III** is stepwise, with the ylide dissociation from heme occurring first *via* $\mathbf{TS_1}$**-III** to form the free ylide $\mathbf{Int_{NC}}$**-III**, followed by two branches to the final product formation. Numerous trials to locate $\mathbf{TS_1}$**-III** were unsuccessful, which is similar to a recent computational work of the dissociation pathway for the Ser-ligated heme carbene N–H insertion.[28] We then conducted potential energy scan (PES) calculations along the Fe–C coordinate for this dissociation process (see ESI† section S6 for details), which were also used in recent heme carbene N–H insertion calculations of similar systems.[41,67,68] Results show that there is an energy cost from both cleaving the Fe–C bond and breaking the hydrogen bond between amine's proton and porphyrin nitrogen, which bears a maximum $\Delta E$ cost of 21.74 kcal mol$^{-1}$ from $\mathbf{Int_{ylide}}$, which was added to all relative energetic terms of $\mathbf{Int_{ylide}}$ to obtain the estimated relative energies for $\mathbf{TS_1}$**-III**. This leads to the relative $\Delta E$ and $\Delta G$ of −26.70 and −7.48 kcal mol$^{-1}$ with respect to starting reactants, as shown in Fig. 2.

After the free ylide $\mathbf{Int_{NC}}$**-III** is formed, we compared the indirect (branch **a**) and direct (branch **b**) pathways to the final product $\mathbf{P_{NH}}$, as shown in Scheme 1.

The rearrangement transition state $\mathbf{TS_{2a}}$**-III** of H′ from N to the carbonyl O to form the free enol $\mathbf{Int_{NC}}$ along branch **a** has a very low relative barrier compared to $\mathbf{Int_{NC}}$**-III** ($\Delta E^{\ddagger}$: 3.02 kcal mol$^{-1}$; $\Delta G^{\ddagger}$: −0.35 kcal mol$^{-1}$, calculated from data in Table S8†), which is much lower compared to the cyclic carbene system ($\Delta E^{\ddagger}$: 9.4 kcal mol$^{-1}$; $\Delta G^{\ddagger}$: 6.4 kcal mol$^{-1}$).[28,29] Then, starting from the enol $\mathbf{Int_{NC}}$, subsequent different enol transformation mechanisms have been studied and discussed above for **Pathway-II**, in which the water-assisted enol rearrangement *via* $\mathbf{TS_{NC}}$**-w** is the most favorable one. As $\mathbf{TS_{NC}}$**-w** is higher than $\mathbf{TS_{2a}}$**-III** to form enol, it is the RDS along this indirect (branch **a**) pathway from free ylide, *i.e.*, branch **a** has the highest $\Delta G$ of −9.61 kcal mol$^{-1}$.

For the direct pathways in branch **b** from free ylide to final product, we also studied them with and without water assistance (see Scheme 1) *via* $\mathbf{TS_{2b}}$**-III** and $\mathbf{TS_{2b}}$**-III-w**, respectively. As found for the cyclic carbene system reported recently,[28] the two-water assisted model with first protonation at the carbene carbon *via* transition state $\mathbf{TS_{2b}}$**-III-w** and subsequent spontaneous deprotonation at the N position to yield product $\mathbf{P_{NH}}$, is of significantly lower energy than the water-free $\mathbf{TS_{2b}}$**-III** by $\Delta G$ of 33.07 kcal mol$^{-1}$ (see Scheme S1†), and thus is the preferred pathway for the direct transformation of free ylide to product along branch **b**.

Since the highest energy species along the favorable direct branch **b** from the free ylide $\mathbf{Int_{NC}}$**-III** is itself (see Fig. 2), it has a relative Gibbs free energy of −13.62 kcal mol$^{-1}$ with respect to reactants and thus lower than the relative Gibbs free energy of −9.61 kcal mol$^{-1}$ for $\mathbf{TS_{NC}}$**-w** (the highest energy species along the indirect branch **a**). As a result, the direct branch **b** is the more favorable one and thus the best **Pathway-III** mechanism. As shown in Fig. 2, this pathway's RDS step is dissociation with a $\Delta G$ of −7.48 kcal mol$^{-1}$, which is of higher energy than the RDS in **Pathway-II** (−9.61 kcal mol$^{-1}$). So, among the first three ylide pathways, **Pathway-II** with RDS of $\mathbf{TS_1}$**-II** is the most preferred one.

In contrast with **Pathway-III**, which features a stepwise mechanism with the initial dissociation of free ylide and then rearrangement to enol as studied for the Cys-ligated heme carbene N–H insertion[41] or direct formation of the final product for the Ser-ligated case,[28] **Pathway-IV** is also stepwise but involves first the rearrangement *via* $\mathbf{TS_1}$**-IV** then dissociation $\mathbf{TS_2}$**-IV** for comparison, see Scheme 1. However, all efforts to locate a pure metal-bound rearrangement $\mathbf{TS_1}$**-IV** of H′ from N to the carbonyl O were optimized to the concerted rearrangement and dissociation transition state $\mathbf{TS_1}$**-II** in the most favorable ylide mechanism **Pathway-II**, as discussed above. This **Pathway-IV** transition state was also absent for the Cys-ligated heme carbene N–H insertion with the same carbene as studied here.[41] In addition, our results show that the lowest energy intermediate $\mathbf{Int_1}$**-IV** after $\mathbf{TS_1}$**-IV** has the Fe–C bond already broken with an $R_{FeC}$ of 3.102 Å, see Table S5.† This further supports that the rearrangement causes simultaneous dissociation and thus this stepwise **Pathway-IV** may not exist.

Overall, these results from heme carbene and substrate to the final products show for the first time that only three out of the four ylide pathways could be successfully located for the His-ligated heme carbene N–H insertion. Fig. 2 collects the branches of each located ylide pathway, which indicates that **Pathway-II** from the metal-bound ylide to enol $\mathbf{Int_{NC}}$ and then *via* water-assisted rearrangement $\mathbf{TS_{NC}}$**-w** to generate the final N–H insertion product is the kinetically most favorable ylide mechanism for the studied acyclic carbene, in contrast with the preferred **Pathway-III** reported for cyclic carbene with Ser-ligated heme.[28]

As seen from Fig. 2, the overall RDS along the favorable ylide pathway here is ylide formation compared to subsequent steps, as found for both Cys- and Ser-ligated heme biocatalytic N–H insertions.[28,41] It has a small barrier and this reaction to the final product formation is also thermodynamically favorable with a net reaction energy of $\Delta G°$ −55.04 kcal mol$^{-1}$, see Fig. 2.

### 3.3 Alternative pathways

Besides the ylide pathways, we also investigated a stepwise HAT mechanism and concerted hydride transfer mechanism for comparison; see Scheme 1.

 

As the hydrogen atom bears radical features, the first transition state $\mathbf{TS_{1HAT}}$ to abstract a hydrogen atom from aniline to carbene carbon displays an OSS feature with $Fe^{III}$ ($S$ = −1/2, spin density of −1.033 e) and shared spin ($S$ = 1/2) between N and C (total spin density is 0.950 e), see Table S11.† This feature can be seen in Fig. 3 for its spin density diagram, in which the transferred H′ atom shows an opposite spin with the remaining aniline and carbene. In the formed intermediate $\mathbf{Int_{HAT}}$, the remaining aniline dissociates with an $R_{CN}$ of 3.963 Å (Table S13†). A subsequent radical rebound leads to the formation of the C–N bond in $\mathbf{TS_{2HAT}}$, which has relatively lower energy compared to $\mathbf{TS_{1HAT}}$ ($\Delta\Delta G$: −9.79 kcal mol$^{-1}$, see Fig. 2). In this step, both C and N again showed radical features, but with opposite spin directions (−0.792 e and 0.648 e, respectively, see Table S11† and Fig. 2), ready for a radical coupling to facilitate the formation of the final product $\mathbf{P_{NH}}$. While the partial C–N bond formation can be seen by its significant distance shortening from 3.963 Å in $\mathbf{Int_{HAT}}$ to 2.581 Å in $\mathbf{TS_{2HAT}}$, a concomitant Fe–C bond elongation of ∼0.6 Å in this step also indicates its partial cleavage, which proceeds to the final release of the product.

As shown in Fig. 3, the RDS barrier ($\Delta G^{\ddagger}$) for the HAT pathway is 13.64 kcal mol$^{-1}$, which is significantly higher than the RDS of the ylide pathway by 13.46 kcal mol$^{-1}$. This shows that the ylide mechanism is more favorable for the His-ligated heme carbene N–H insertion based on a complete reaction pathway to the final product formation, which is the same as found previously for the Cys-ligated system[41] based on the first-step comparisons.

We also attempted the concerted nonsynchronous hydride transfer with C–N bond formation and Fe–C dissociation mechanism as found in prior studies for the heme carbene catalyzed C–H/Si–H insertion reactions.[36,43,44] However, all attempts to get this transition state $\mathbf{TS_{Hydride}}$ were optimized as either the concerted proton H′ transfer from N to C with the Fe–C bond dissociation $\mathbf{TS_1}$-**I** in the ylide pathway or $\mathbf{TS_{1HAT}}$ in the HAT pathway, suggesting that the hydride pathway is not favorable here. This may be a result of the much higher electronegativity of N *vs.* C/Si, which makes it difficult to form hydride from an N–H bond.

### 3.4 Mechanistic features of the overall RDS

Based on the above systematic mechanism study, the ylide **Pathway-II** is most favorable for His-ligated heme carbene N–H insertion and the overall RDS is ylide formation. The key geometry and charge changes with respect to reactants were analyzed, which were found to be useful to understand the mechanistic features of this RDS step as reported recently for the heme carbene cyclopropanation and C–H/Si–H insertions.[43,44,47] As shown in Fig. 4A, the largest geometric change is the partial formation of a C–N bond in $\mathbf{TS_{ylide}}$, with visible shortening of the Fe–His bond (∼−0.03 Å) to push the carbene away (elongation of ∼0.03 Å in Fe–C bond length) *via* the axial ligand's *trans* effect to facilitate its attack of the

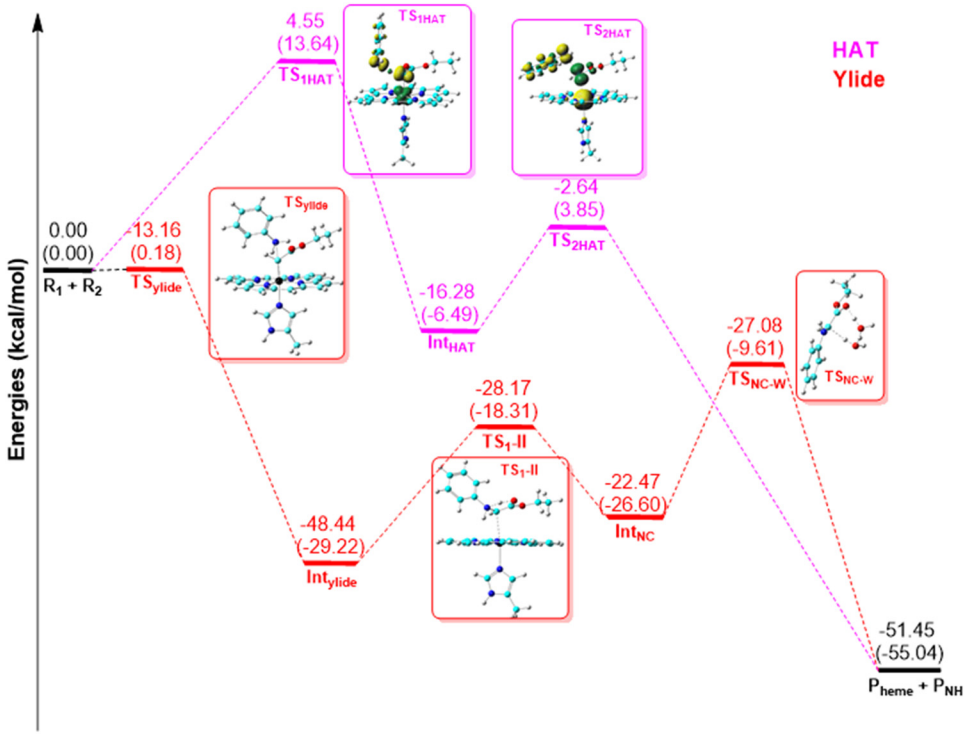


Fig. 3 Energy diagrams for the most favorable steps in the ylide and HAT pathways of heme-carbene catalyzed N–H insertions, where the energy levels are based on $\Delta G$. Relative $\Delta E$ and $\Delta G$ energies (in kcal mol$^{-1}$) are outside and inside the parenthesis, respectively. Transition state structures are shown. The spin densities are shown for $\mathbf{TS_{1HAT}}$ and $\mathbf{TS_{2HAT}}$. Contour values = ±0.01 au.

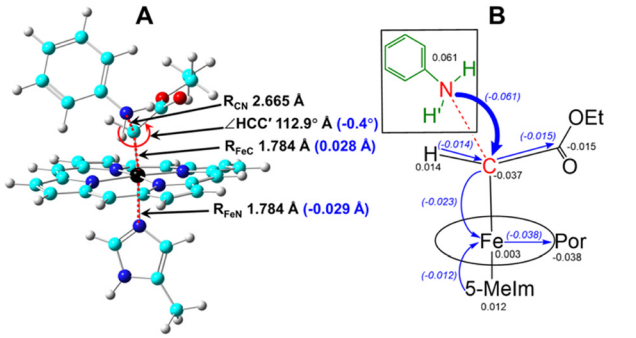


Fig. 4 A) Key geometric parameters of $TS_{ylide}$ (in black) and geometry changes (in blue) from reactants ($R_1$ and $R_2$) to $TS_{ylide}$. C′ is carbonyl carbon. B) Atomic charge changes (unit: e) from reactants to $TS_{ylide}$ in black. Charge transfer is indicated by arrows and numbers in parentheses. Substrate aniline is shown in the box. Oval represents porphyrin.

substrate. In this transition state, the N–H bond length change (≤0.003 Å) from substrate $\mathbf{R_2}$ is negligible compared to its difference (≥0.01 Å) with respect to the formed $\mathbf{Int_{ylide}}$; see data in Table S9.† This suggests an early transition state feature for this RDS. As demonstrated in Fig. 4B, the largest charge transfer is from the aniline substrate to heme carbene (0.061 e), exhibiting the electrophilicity of carbene, which leads to a negatively charged carbene carbon. However, this charge transfer is significantly smaller than that for many heme carbene cyclopropanation and C–H/Si–H insertions,[43,44,47] which are mostly around 0.3–0.4 e for concerted nonsynchronous reaction mechanisms. These results suggest that heme carbene N–H insertions have a distinctive ylide mechanism, and the effects of electronic features of substrates may be less significant than the electrophilic heme carbene cyclopropanation and C–H/Si–H insertions,[43,44,47] while the reactant steric effect may affect the reactivity *via* its influence to the metal-bound ylide formation in RDS. These features are consistent with experimental data that both electron-donating and electron-withdrawing substrates are tolerated, and bulky reactants have relatively lower yields in heme-catalyzed N–H insertions.[27,28,32–34,37,38,40]

## 4. Experimental mechanistic investigation

In a previous study, an engineered active site variant of sperm whale myoglobin, Mb(H64V,V68A), was determined to catalyze an N–H carbene insertion reaction between aniline and ethyl α-diazoacetate (EDA) and ethyl 2-diazopropanoate (EDP) with up to 6150 TON and 130 TON, respectively.[34] To investigate their radical *vs.* non-radical nature, these N–H insertion reactions were carried out in the presence and in the absence of the radical spin trapping agent 5,5-dimethyl-1-pyrroline *N*-oxide (DMPO). In the previously published work, we successfully applied DMPO to probe the radical mechanism of an engineered myoglobin biocatalyst for another carbene transfer reaction (cyclopropanation): the DMPO-dependent inhibition was observed, and the radical intermediate is bound to the enzyme. The success of those experiments gives us confidence that the DMPO is a suitable probe for trapping the long-lived intermediate in this system if formed.[75] As shown in Table 1, no effect in product yield

Table 1 Catalytic activity of myoglobin variants and transition metal catalysts in the N–H insertion reaction with diazo compounds in the presence and absence of a radical trap reagent[a]

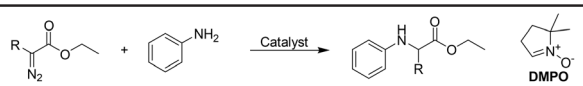


| Entry | Catalyst | (R) | DMPO[b] | Yield[c,d] (%) |
|---|---|---|---|---|
| 1 | Mb | H | No | 66 (±3) |
| 2 | Mb | H | Yes | 60 (±3) |
| 3 | Mb(H64V, V68A) | H | No | 79 (±4) |
| 4 | Mb(H64V, V68A) | H | Yes | 81 (±6) |
| 5 | Hemin | H | No | 47 (±2) |
| 6 | Hemin | H | Yes | 49 (±4) |
| 7 | Co(TPP)[B] | H | No | 60 (±3) |
| 8 | Co(TPP)[B] | H | Yes | 2 (±1) |
| 9 | Mb | Me | No | 65 (±4) |
| 10 | Mb | Me | Yes | 63 (±2) |
| 11 | Mb(H64V, V68A) | Me | No | 51 (±3) |
| 12 | Mb(H64V, V68A) | Me | Yes | 42 (±4) |
| 13 | Hemin | Me | No | 32 (±1) |
| 14 | Hemin | Me | Yes | 33 (±5) |
| 15 | Co(TPP)[B] | Me | No | 54 (±1) |
| 16 | Co(TPP)[B] | Me | Yes | 3 (±1) |

[a] Reaction conditions: 5 mM aniline, 10 mM diazo compound, 10 μM Mb variant (or hemin), 10 mM sodium dithionite in 50 mM potassium phosphate buffer (pH 7) containing 10% DMF or 50 mM DMPO, room temp., 1 hour, anaerobic conditions. Reaction conditions B: 0.24 mmol aniline, 1.5 equiv. diazo compound, 5 mol% Co(TPP) in toluene, 60 °C, 16 hours, anaerobic conditions. [b] With or without 10 equiv. DMPO relative to styrene. [c] GC yields calculated using calibration curves with authentic standards. [d] Standard deviations calculated from triplicate experiments.

was observed for the reactions with EDA catalyzed by wild-type myoglobin, Mb(H64V,V68A), or hemin in the presence of DMPO when compared to parallel reactions performed in the absence of the spin trapping reagent (entries 1, 3, and 5 *vs.* 2, 4, and 6, respectively). In contrast, a dramatic reduction in product yield (~90% reduction) was observed for the Co(TPP)-catalyzed reaction in the presence of the radical trapping reagent (entry 7 *vs.* 8), which is consistent with the radical reactivity of this catalyst.[76] Similar results are observed in the N–H insertion reaction of aniline and EDP (entries 9, 11, and 13 *vs.* 10, 12, and 15, respectively). These results thus agree with those obtained from our computational analyses in supporting a non-radical mechanism for hemoprotein-catalyzed N–H insertion.

## 5. Conclusions

This work provides a most comprehensive mechanistic investigation of heme carbene N–H insertion with many pathway comparisons revealed for the first time, as briefly summarized at the end of the Introduction. Regarding the electronic structure of the involved heme carbene from the widely used precursor EDA, it was found to have a CSS ground state based on high-level CASSCF calculations, consistent with prior CASSCF works on similar heme carbenes[52] and computational predictions of their experimental spectroscopic properties[44,50] as well as related experimental works.[51] Results show that the HAT and hydride transfer mechanisms are less favorable than the ylide pathway, which has four main sub-pathways with a number of subsequent branches. Overall, the most favorable pathway for the His-ligated heme catalyzed N–H insertion with the acyclic carbene studied here starts with the formation of a metal-bound ylide, then undergoes a concerted rearrangement of ylide to enol and dissociation of the Fe–C bond, and finally generate the N–H insertion product *via* the water-assisted rearrangement of enol. The preference for the ylide pathway over the HAT mechanism found in the above systematic computational study was further supported by the additional experimental work. A detailed analysis of the geometric and electronic features of the overall RDS (ylide formation) shows that this reaction is of mild electrophilicity, and the steric effect may also influence reactivity. Future studies to include the whole protein will be performed to offer a more detailed understanding of the effect of the protein environment on such biocatalytic reactions. Given that 79% of the experimental biocatalytic heme N–H insertions employ the cofactor with a His axial ligand and 86% of the experimental work in this area utilized acyclic carbenes,[27–40] the novel and significant mechanistic results here will facilitate future heme-based biocatalytic N–H insertion research for sustainable chemical synthesis.

## Data availability

The authors declare that the data supporting the findings of this study are available within the paper and its ESI† files.

## Author contributions

Y. Z. conceived the idea and designed the research. R. L. K., X. Z., and C. W. conducted the computational studies. R. D. A. performed the experimental work under the guidance and supervision of R. F. All authors participated in the data analyses and preparation of data tables and figures. R. L. K. and Y. Z. wrote the manuscript with input and additions from all other co-authors.

## Conflicts of interest

There are no conflicts to declare.

## Acknowledgements

This work was supported by a U.S. National Science Foundation grant CHE-2054897 to Y. Z and a U. S. National Institute of Health GM098628 to R. F. R. F. acknowledges chair endowment support from the Robert A. Welch Foundation (Chair, AT-0051).

## References

1 C. Bolm, A. Kasyan, K. Drauz, K. Günther and G. Raabe, *Angew. Chem., Int. Ed.*, 2000, **39**, 2288–2290.
2 F. A. Davis, T. Fang and R. Goswami, *Org. Lett.*, 2002, **4**, 1599–1602.
3 K. Yamazaki and Y. Kondo, *Chem. Commun.*, 2002, 210–211.
4 K. E. Bashford, A. L. Cooper, P. D. Kane, C. J. Moody, S. Muthusamy and E. Swann, *J. Chem. Soc., Perkin Trans. 1*, 2002, 1672–1687.
5 S.-H. Lee, B. Clapham, G. Koch, J. Zimmermann and K. D. Janda, *J. Comb. Chem.*, 2003, **5**, 188–196.
6 A. C. B. Burtoloso and C. R. D. Correia, *Tetrahedron Lett.*, 2004, **45**, 3355–3358.
7 J. R. Davies, P. D. Kane and C. J. Moody, *Tetrahedron*, 2004, **60**, 3967–3977.
8 H. Matsushita, S.-H. Lee, K. Yoshida, B. Clapham, G. Koch, J. Zimmermann and K. D. Janda, *Org. Lett.*, 2004, **6**, 4627–4629.
9 I. Aviv and Z. Gross, *Chem. Commun.*, 2006, 4477–4479.
10 B. Liu, S.-F. Zhu, W. Zhang, C. Chen and Q.-L. Zhou, *J. Am. Chem. Soc.*, 2007, **129**, 5834–5835.
11 M. E. Morilla, M. M. Díaz-Requejo, T. R. Belderrain, M. C. Nicasio, S. Trofimenko and P. J. Pérez, *Chem. Commun.*, 2002, 2998–2999.
12 J. R. Davies, P. D. Kane and C. J. Moody, *J. Org. Chem.*, 2005, **70**, 7305–7316.
13 J. Bariwal and E. Van der Eycken, *Chem. Soc. Rev.*, 2013, **42**, 9283–9303.
14 H. Kohls, F. Steffen-Munsberg and M. Höhne, *Curr. Opin. Chem. Biol.*, 2014, **19**, 180–192.
15 J. E. Kim, S. Choi, M. Balamurugan, J. H. Jang and K. T. Nam, *Trends Chem.*, 2020, **2**, 1004–1019.
16 Y. Chen, R. Zhang, Z. Chen, J. Liao, X. Song, X. Liang, Y. Wang, J. Dong, C. V. Singh, D. Wang, Y. Li, F. D. Toste and J. Zhao, *J. Am. Chem. Soc.*, 2024, **146**, 10847–10856.

17 S. Harada, S. Hirose, M. Takamura, M. Furutani, Y. Hayashi and T. Nemoto, *J. Am. Chem. Soc.*, 2024, **146**, 733–741.
18 D. Gillingham and N. Fei, *Chem. Soc. Rev.*, 2013, **42**, 4918–4931.
19 J. M. Antos and M. B. Francis, *J. Am. Chem. Soc.*, 2004, **126**, 10256–10257.
20 C.-M. Ho, J.-L. Zhang, C.-Y. Zhou, O.-Y. Chan, J. J. Yan, F.-Y. Zhang, J.-S. Huang and C.-M. Che, *J. Am. Chem. Soc.*, 2010, **132**, 1886–1894.
21 K. Tishinov, K. Schmidt, D. Häussinger and D. G. Gillingham, *Angew. Chem., Int. Ed.*, 2012, **51**, 12000–12004.
22 L. K. Baumann, H. M. Mbuvi, G. Du and L. K. Woo, *Organometallics*, 2007, **26**, 3995–4002.
23 I. Aviv and Z. Gross, *Chem. – Eur. J.*, 2008, **14**, 3995–4005.
24 P. Le Maux, I. Nicolas, S. Chevance and G. Simonneaux, *Tetrahedron*, 2010, **66**, 4462–4468.
25 H. X. Wang, Q. Wan, K. H. Low, C. Y. Zhou, J. S. Huang, J. L. Zhang and C. M. Che, *Chem. Sci.*, 2020, **11**, 2243–2259.
26 C. Ma, S. Wang, Y. Sheng, X. L. Zhao, D. Xing and W. Hu, *J. Am. Chem. Soc.*, 2023, **145**, 4934–4939.
27 Z. J. Wang, N. E. Peck, H. Renata and F. H. Arnold, *Chem. Sci.*, 2014, **5**, 598–601.
28 Z. Liu, C. Calvo-Tusell, A. Z. Zhou, K. Chen, M. Garcia-Borras and F. H. Arnold, *Nat. Chem.*, 2021, **13**, 1166–1172.
29 C. Calvo-Tusell, Z. Liu, K. Chen, F. H. Arnold and M. Garcia-Borras, *Angew. Chem., Int. Ed.*, 2023, **62**, e202303879.
30 E. J. Moore, V. Steck, P. Bajaj and R. Fasan, *J. Org. Chem.*, 2018, **83**, 7480–7490.
31 G. Sreenilayam, E. J. Moore, V. Steck and R. Fasan, *Adv. Synth. Catal.*, 2017, **359**, 2076–2089.
32 G. Sreenilayam and R. Fasan, *Chem. Commun.*, 2015, **51**, 1532–1534.
33 V. Steck, G. Sreenenilayam and R. Fasan, *Synlett*, 2020, **31**, 224–229.
34 V. Steck, D. M. Carminati, N. R. Johnson and R. Fasan, *ACS Catal.*, 2020, **10**, 10967–10977.
35 M. Pott, M. Tinzl, T. Hayashi, Y. Ota, D. Dunkelmann, P. R. E. Mittl and D. Hilvert, *Angew. Chem., Int. Ed.*, 2021, **60**, 15063–15068.
36 M. Garcia-Borras, S. B. J. Kan, R. D. Lewis, A. Tang, G. Jimenez-Oses, F. H. Arnold and K. N. Houk, *J. Am. Chem. Soc.*, 2021, **143**, 7114–7123.
37 D. Nam, A. Tinoco, Z. Shen, R. D. Adukure, G. Sreenilayam, S. D. Khare and R. Fasan, *J. Am. Chem. Soc.*, 2022, **144**, 2590–2602.
38 V. S. Alfaro, S. O. Waheed, H. Palomino, A. Knorrscheidt, M. Weissenborn, C. Z. Christov and N. Lehnert, *Chem. – Eur. J.*, 2022, **28**, e202201474.
39 N. J. Porter, E. Danelius, T. Gonen and F. H. Arnold, *J. Am. Chem. Soc.*, 2022, **144**, 8892–8896.
40 L. J. Sun, H. Wang, J. K. Xu, S. Q. Gao, G. B. Wen and Y. W. Lin, *Inorg. Chem.*, 2023, **62**, 16294–16298.
41 D. A. Sharon, D. Mallick, B. Wang and S. Shaik, *J. Am. Chem. Soc.*, 2016, **138**, 9597–9610.
42 Y. Zhang, *Chem. – Eur. J.*, 2019, **25**, 13231–13247.
43 R. L. Khade, A. L. Chandgude, R. Fasan and Y. Zhang, *ChemCatChem*, 2019, **11**, 3101–3108.
44 R. L. Khade and Y. Zhang, *Chem. – Eur. J.*, 2017, **23**, 17654–17658.
45 Y. Wei, M. Conklin and Y. Zhang, *Chem. – Eur. J.*, 2022, **28**, e202202006.
46 R. L. Khade and Y. Zhang, *J. Am. Chem. Soc.*, 2015, **137**, 7560–7563.
47 Y. Wei, A. Tinoco, V. Steck, R. Fasan and Y. Zhang, *J. Am. Chem. Soc.*, 2018, **140**, 1649–1662.
48 Y. Shi and Y. Zhang, *Angew. Chem., Int. Ed.*, 2018, **57**, 16654–16658.
49 K. Chen, S. Q. Zhang, O. F. Brandenberg, X. Hong and F. H. Arnold, *J. Am. Chem. Soc.*, 2018, **140**, 16402–16407.
50 R. L. Khade, W. Fan, Y. Ling, L. Yang, E. Oldfield and Y. Zhang, *Angew. Chem., Int. Ed.*, 2014, **53**, 7574–7578.
51 Y. Liu, W. Xu, J. Zhang, W. Fuller, C. E. Schultz and J. Li, *J. Am. Chem. Soc.*, 2017, **139**, 5023–5026.
52 G. D. Stroscio, M. Srnec and R. G. Hadt, *Inorg. Chem.*, 2020, **59**, 8707–8715.
53 D. A. Vargas, R. L. Khade, Y. Zhang and R. Fasan, *Angew. Chem., Int. Ed.*, 2019, **58**, 10148–10152.
54 D. Nam, J. P. Bacik, R. L. Khade, M. C. Aguilera, Y. Wei, J. D. Villada, M. L. Neidig, Y. Zhang, N. Ando and R. Fasan, *Nat. Commun.*, 2023, **14**, 7985.
55 A. Tinoco, Y. Wei, J. P. Bacik, E. J. Moore, N. Ando, Y. Zhang and R. Fasan, *ACS Catal.*, 2019, **9**, 1514–1524.
56 G. D. Stroscio, M. Srnec and R. G. Hadt, *Inorg. Chem.*, 2020, **59**, 8707–8715.
57 X. Li, L. Dong and Y. Liu, *Inorg. Chem.*, 2020, **59**, 1622–1632.
58 S. E. Stavretis, M. Atanasov, A. A. Podlesnyak, S. C. Hunter, F. Neese and Z.-L. Xue, *Inorg. Chem.*, 2015, **54**, 9790–9801.
59 W. J. Yang, X. B. Chen, H. Z. Su, W. H. Fang and Y. Zhang, *Chem. Commun.*, 2015, **51**, 9616–9619.
60 M. J. Frisch, G. W. Trucks, H. B. Schlegel, G. E. Scuseria, M. A. Robb, J. R. Cheeseman, G. Scalmani, V. Barone, G. A. Petersson, H. Nakatsuji, X. Li, M. Caricato, A. V. Marenich, J. Bloino, B. G. Janesko, R. Gomperts, B. Mennucci, H. P. Hratchian, J. V. Ortiz, A. F. Izmaylov, J. L. Sonnenberg, D. Williams-Young, F. Ding, F. Lipparini, F. Egidi, J. Goings, B. Peng, A. Petrone, T. Henderson, D. Ranasinghe, V. G. Zakrzewski, J. Gao, N. Rega, G. Zheng, W. Liang, M. Hada, M. Ehara, K. Toyota, R. Fukuda, J. Hasegawa, M. Ishida, T. Nakajima, Y. Honda, O. Kitao, H. Nakai, T. Vreven, K. Throssell, J. A. Montgomery Jr , J. E. Peralta, F. Ogliaro, M. J. Bearpark, J. J. Heyd, E. N. Brothers, K. N. Kudin, V. N. Staroverov, T. A. Keith, R. Kobayashi, J. Normand, K. Raghavachari, A. P. Rendell, J. C. Burant, S. S. Iyengar, J. Tomasi, M. Cossi, J. M. Millam, M. Klene, C. Adamo, R. Cammi, J. W. Ochterski, R. L. Martin, K. Morokuma, O. Farkas, J. B. Foresman and D. J. Fox, *Gaussian 16, Revision C.01*, Gaussian, Inc., Wallingford CT, 2019.
61 B. Mennucci and J. Tomasi, *J. Chem. Phys.*, 1997, **106**, 5151–5158.
62 R. A. Torres, T. Lovell, L. Noodleman and D. A. Case, *J. Am. Chem. Soc.*, 2003, **125**, 1923–1936.

 

63 M. R. A. Blomberg, T. Borowski, F. Himo, R.-Z. Liao and P. E. M. Siegbahn, *Chem. Rev.*, 2014, **114**, 3601–3658.
64 Y. Shi, M. A. Michael and Y. Zhang, *Chem. – Eur. J.*, 2021, **27**, 5019–5027.
65 J.-D. Chai and M. Head-Gordon, *Phys. Chem. Chem. Phys.*, 2008, **10**, 6615–6620.
66 P. J. Hay and W. R. Wadt, *J. Chem. Phys.*, 1985, **82**, 270–283.
67 Z. Liu, C. Calvó-Tusell, A. Z. Zhou, K. Chen, M. Garcia-Borràs and F. H. Arnold, *Nat. Chem.*, 2021, **13**, 1166–1172.
68 C. Calvó-Tusell, Z. Liu, K. Chen, F. H. Arnold and M. Garcia-Borràs, *Angew. Chem., Int. Ed.*, 2023, **62**, e202303879.
69 J.-C. Wang, Z.-J. Xu, Z. Guo, Q.-H. Deng, C.-Y. Zhou, X.-L. Wan and C.-M. Che, *Chem. Commun.*, 2012, **48**, 4299–4301.
70 K.-H. Chan, X. Guan, V. K.-Y. Lo and C.-M. Che, *Angew. Chem., Int. Ed.*, 2014, **53**, 2982–2987.
71 E. Nakamura, N. Yoshikai and M. Yamanaka, *J. Am. Chem. Soc.*, 2002, **124**, 7181–7192.
72 M. J. Frisch, G. W. Trucks, H. B. Schlegel, G. E. Scuseria, M. A. Robb, J. R. Cheeseman, G. Scalmani, V. Barone, B. Mennucci, G. A. Petersson, H. Nakatsuji, M. Caricato, X. Li, H. P. Hratchian, A. F. Izmaylov, J. Bloino, G. Zheng, J. L. Sonnenberg, M. Hada, M. Ehara, K. Toyota, R. Fukuda, J. Hasegawa, M. Ishida, T. Nakajima, Y. Honda, O. Kitao, H. Nakai, T. Vreven, J. A. Montgomery Jr , E. J. Peralta, F. Ogliaro, M. Bearpark, J. J. Heyd, E. Brothers, K. N. Kudin, V. N. Staroverov, T. Keith, R. Kobayashi, J. Normand, K. Raghavachari, A. Rendell, J. C. Burant, S. S. Iyengar, J. Tomasi, M. Cossi, N. Rega, J. M. Millam, M. Klene, J. E. Knox, J. B. Cross, V. Bakken, C. Adamo, J. Jaramillo, R. Gomperts, R. E. Stratmann, O. Yazyev, A. J. Austin, R. Cammi, C. Pomelli, J. W. Ochterski, R. L. Martin, K. Morokuma, V. G. Zakrzewski, G. A. Voth, P. Salvador, J. J. Dannenberg, S. Dapprich, A. D. Daniels, O. Farkas, J. B. Foresman, J. V. Ortiz, J. Cioslowski and D. J. Fox, *Gaussian 09, Revision B.01*, Gaussian, Inc., Wallingford CT, 2010.
73 P. G. Blachly, G. M. Sandala, D. A. Giammona, D. Bashford, J. A. McCammon and L. Noodleman, *Inorg. Chem.*, 2015, **54**, 6439–6461.
74 X.-C. Wang, X.-S. Song, L.-P. Guo, D. Qu, Z.-Z. Xie, F. Verpoort and J. Cao, *Organometallics*, 2014, **33**, 4042–4050.
75 D. M. Carminati and R. Fasan, *ACS Catal.*, 2019, **9**, 9683–9697.
76 H. Lu, W. I. Dzik, X. Xu, L. Wojtas, B. de Bruin and X. P. Zhang, *J. Am. Chem. Soc.*, 2011, **133**, 8518–8521.